

Study of the electrical characteristics of CdZnTe Schottky diodes

E. Gaubas^{a,*}, T. Ceponis^a, L. Deveikis^a, V. Kalesinskas^a, G. Kreiza^a, T. Malinauskas^a, J. Pavlov^a, V. Rumbauskas^a, A. Mychko^b, V. Ivanov^c

^a Institute of Photonics and Nanotechnology, Vilnius University, Sauletekio Av. 3, LT-10257, Vilnius, Lithuania

^b Riga Technical University, 3 Paula Valdena Str., LV-1048, Riga, Latvia

^c ZRF RITEC SIA, Gustava Zemgala Str. 71A, LV-1039, Riga, Latvia

ABSTRACT

Cadmium zinc telluride (CZT) is a promising material for the room temperature detection and spectroscopy of ionizing radiations. Two sets of samples, exhibiting good and unacceptable performance of CZT radiation detectors, have been studied in order to resolve difference in the electrical and structural parameters which govern operational characteristics of CZT detectors. I–V, barrier capacitance, carrier lifetime, and drift velocity measurements have been combined to reveal the main differences in electrical characteristics which determine crucial difference in spectral performance of CZT radiation detectors.

1. Introduction

Cadmium zinc telluride (CZT) is a promising material for the room temperature X- and gamma-ray detectors due to high average atomic number providing high stopping power as well as rather large band-gap which determines large resistivity, small leakage-current, and good energy resolution [1–3]. CZT detectors are desirable in applications such as tomography, X-ray radiology, X-ray CT scan and X-ray imaging [4], space and astronomy [5], defence and homeland security [6]. The growth process of the high quality ternary CZT crystals is complicated, because the defects distribution and stoichiometry differ along the same ingot. The prevailing defects in CZT crystals are Cd vacancies (V_{Cd}) and A-centres occurring in CZT [1–3,7]. Many reports had been published on analysis of relation between the detector performance and the nature of the defects which dominate carrier recombination parameters [7–12]. The carrier transport properties that have the decisive impact on the compensation phenomena and detector performance also are not perfectly understood yet. It had been previously believed that the presence of A-centres explains the high resistance in the compensated CZT materials [2,13,14]. It is reported that some dopants form complex defects which cause reduction of carrier mobility. However, origin and activation energy parameters are not fully understood yet [15–24]. The high density of the mentioned defects leads to the significant decrease of the parameters, characterizing charge collection, due to capture and recombination processes, and energy resolution of CZT detectors operating with intensive radiation fluxes. Under high irradiation flux, the trapped charge accumulates inside the detector, affecting its stability, causing polarization of the detector and other electrical characteristics.

In this work, two sets of samples, exhibiting different performance

of CZT radiation detectors, have been studied in order to resolve difference in the electrical and structural parameters which govern operational characteristics of CZT detectors. Several techniques, such as I–V, barrier capacitance, carrier lifetime and drift velocity measurements, have been combined to reveal the main differences in electrical characteristics which determine crucial difference in spectral performance of CZT radiation detectors.

2. Material and diode structures

Two sets of CdZnTe (CZT) p-type material have been examined. CZT crystals were grown by the Traveling Heater Method (THM) technology. The samples were cut of the commercially available CZT materials addressed to fabrication of the quasi hemispherical detectors. The samples of about $3 \times 3 \times 1.5 \text{ mm}^3$ dimensions were made with mechanically polished surfaces of optical quality. The polishing procedure was performed by gradual reducing of the grain size. This procedure was finalized by etching in a bromine-methanol solution. The diodes were fabricated by deploying In to get a Schottky junction on p-type material and Au to form an ohmic contact. The capacitance characteristics of these diodes measured in dark appeared to be nearly independent of applied reverse voltage, and this implied the high resistivity of these materials. The prevailing p-type conductivity was evaluated according to polarity of the diode reverse/forward voltage in measurements of the inherent I–V, barrier capacitance and transient current characteristics. The typical features of these two batches of materials have been analysed by comparing the inherent characteristics obtained on two samples taken from the examined sample sets. All the measurements were performed on the same sample of the set using both

* Corresponding author.

E-mail address: eugenijus.gaubas@ff.vu.lt (E. Gaubas).

<https://doi.org/10.1016/j.mssp.2019.104705>

Received 14 June 2019; Received in revised form 26 August 2019; Accepted 29 August 2019

Available online 31 August 2019

1369-8001/ © 2019 Elsevier Ltd. All rights reserved.

contact and non-metallized areas, surrounding contacts, when the contactless methods were applied.

2.1. Spectra of radiation detection

The quasi-hemispherical detectors [25,26] of size $3 \times 3 \times 1.5 \text{ mm}^3$ were fabricated, using the same samples, and tested in a high gamma-radiation flux of ^{137}Cs . Such detectors are rectangular with a length-width-height ratio of $A \times A \times (A/2)$. The quasi-hemispherical detectors have large negative electrode on five sides and a positive dot electrode in the centre of one of the large sides.

The gamma-radiation source ^{137}Cs was mounted within lead container. The spectroscopy setup with a calibrated measurement bench, which allows varying of a distance between the source and the detector (thereby, the irradiation flux), was exploited. The detector mounted in the fixture was connected to the input of a charge-sensitive pre-amplifier. The signals from the output of the charge-sensitive pre-amplifier were transferred to the input of a digital multi-channel analyser MCA-527, GBS-Elektronik GmbH. The detector was fed from the inside high voltage power supply of the MCA-527. Equivalent of $1 \mu\text{s}$ shaping time was used. The exposure in high flux gamma-radiation fields was kept 1 s, while the counting rate was of about 300–400 kcps. The MCA-527 circuit performed the dead time correction.

The tested detectors differ in spectroscopy performance (Fig. 1): one of them (N220) showed good energy resolution (with narrow FWHM peaks, Fig. 1a). For instance, a clear peak positioned between 40 and 48

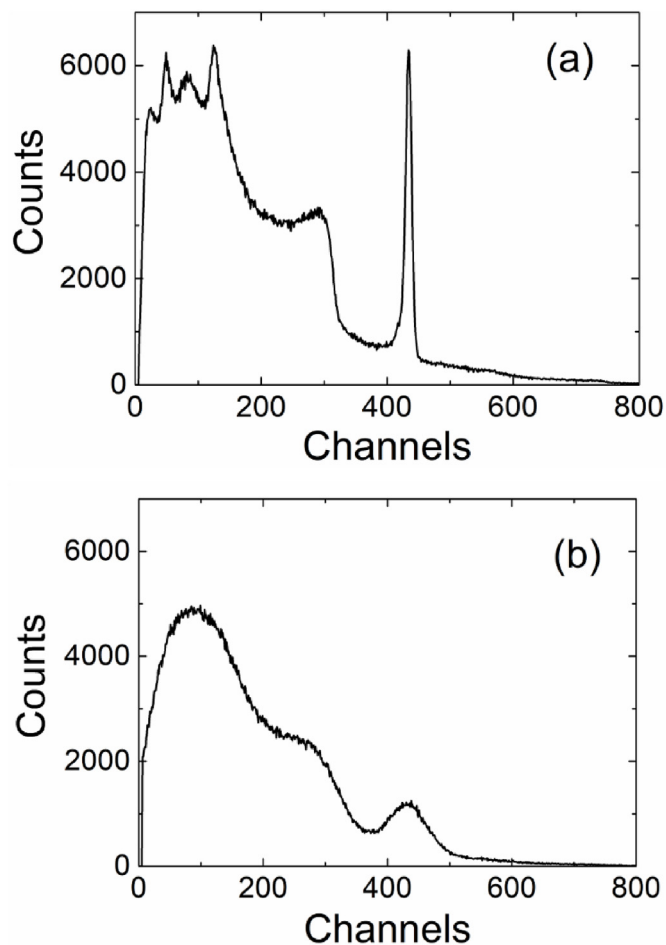


Fig. 1. ^{137}Cs spectra recorded using detector N220 (a), (FWHM @ 662 keV–17.3 keV) and detector N201 (b) (FWHM @ 662 keV–84 keV) at the same test conditions: detector operating voltage – 600 V, gamma-radiation field with dose rate about 0.5 Sv/h.

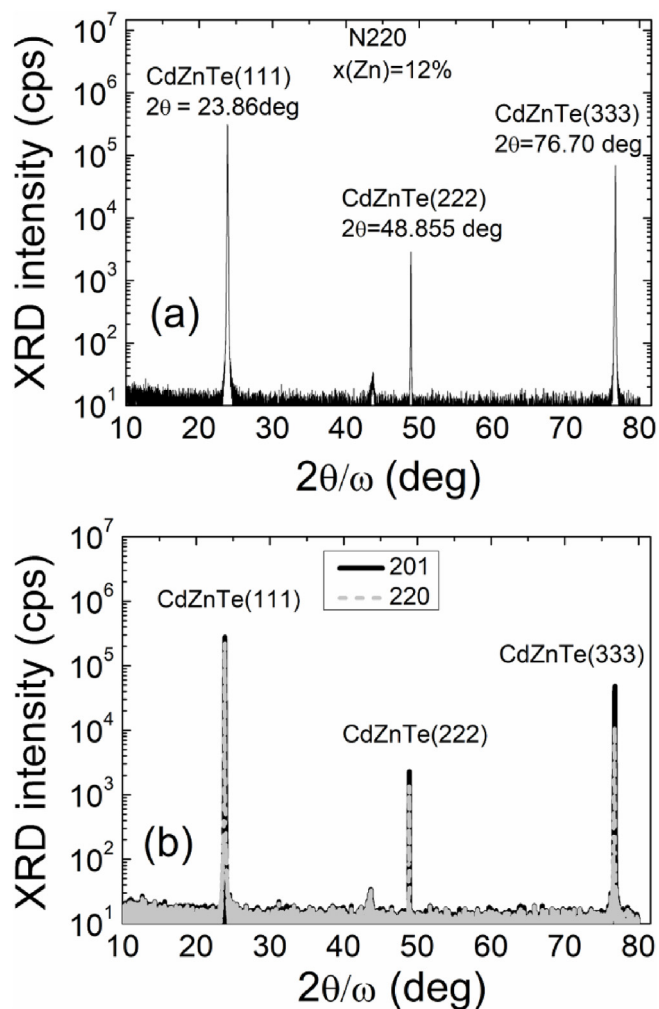


Fig. 2. (a)- The XRD spectrum recorded on sample N220. (b)- The comparison of XRD spectra obtained for both type samples N220 and N201.

channels (Fig. 1a) can be observed, which corresponds to the energy of about 74 keV. This peak is formed by two overlapped lead components ($\text{Pb } K_{\alpha 1} - 72.8 \text{ keV}$ and $\text{Pb } K_{\alpha 2} 75.0 \text{ keV}$) within a characteristic X-ray spectrum, due to lead container where gamma-radiation source ^{137}Cs is mounted. Also, a weak line (channel 22, Fig. 1a) at 33 keV of ^{137}Cs appears.

While, another (N201) detector showed low energy resolution (Fig. 1b). The above mentioned lines at 22 and 40–48 channels are not distinguishable for N201 detector, because of the high threshold level automatically set by the multi-channel analyser (MCA-527). The high threshold level was defined by a high noise level and too long rise times of the output pulses. Additionally, the electrical instabilities and clear quenching of photoconductivity have been observed for this type detectors.

2.2. XRD characteristics

The crystalline quality of the CdZnTe (CZT) material was inspected by X-ray diffraction (XRD) technique, using a high resolution (HRXRD) Rigaku SmartLab instrument. The narrow peaks of symmetrical $\omega/2\theta$ scans (Fig. 2) ascribed to different crystal planes indicated high quality of a single crystal structure and confirmed (111) surface orientation of the samples. The XRD spectra for both type samples coincide (Fig. 2b).

FWHM's of XRD ω -scans were below $90''$ confirming good crystal quality and indicated low density (below resolution threshold) of dislocations. By combining XRD and EDXS characteristics, the Cd and Zn

Table 1
Elements in the examined sets of CdZnTe material resolved by EDXS.

Samples	C (%)	O (%)	Al (%)	Zn (%)	Cd (%)	Te (%)
N201	16.14	2.49	5.35	5.12	36.42	34.48
N220	13.30	–	5.53	3.25	37.53	40.39

components within $\text{Cd}_{1-x}\text{Zn}_x\text{Te}$ ternary compound were determined to be $x = 0.12$ for N220 material samples and $x = 0.13$ for N201 material, respectively. This indicated that the samples are nearly the same $\text{Cd}_{1-x}\text{Zn}_x\text{Te}$ ternary compounds.

2.3. SEM and EDXS characteristics

The surface state of samples was evaluated by scanning electron microscopy (SEM) using a Hitachi SU8230 instrument. Also, the prevailing elements were selected by using energy dispersed X-ray spectroscopy (EDXS) using this SEM equipped with an EDX Bruker spectrometer. The metallization-free contact surrounding areas were examined. The samples were mounted on SEM measurement stage by using double-sided copper adhesive tape. The organic pollution removal and nitrogen gas blowing was applied in preparing of the diode samples for SEM and EDXS analysis. A few scans were made on cleft surface.

The percentage content of elements comprising the single-crystals as well as impurities were evaluated by averaging of the EDX spectra taken in several locations. These resolved elements are listed in Table 1.

The impurities of carbon (C), oxygen (O) and aluminum (Al) have been detected in the N201 set of samples, as can be deduced from Table 1. While, only C and Al elements were resolved in the N220 set. An elemental Al might appear from metallization procedures in formation of contacts and wires, as EDXS measurements were made on device structures. C and O elements can be a residual pollution of surfaces. Moreover, EDXS resolution for C and O elements was close to threshold.

A flat surface with several dark areas has been observed in SEM images taken for the N220 set samples (Fig. 3a). The similar areas of enhanced density can also be found in SEM image for the N201 sample (Fig. 3b). The enhanced amount of Te (of about 51% for N201 and 62% for N220 samples, respectively) was detected by EDXS scans performed on dark area locations. These dark areas in Fig. 3b are decorated with a granular structure of bright spots which are distributed nearly homogeneously, as illustrated in the inset for Fig. 3b. The dark areas can be attributed to large-size and rather small concentration of Te inclusions formed during growth of CZT crystal. It had been observed the similar structures of Te inclusions [27–29] comprising either enhanced area/small density or rather small area/large concentration Te inclusions, which modify characteristics of ionizing radiation detectors. Thereby, the examined CZT samples seem to differ in Te inclusion amount and structure. Additionally, Fourier Transformed Infra-Red (FTIR) spectroscopy (results will be published elsewhere) performed in the range of 1–16 μm on these samples showed existence of Te precipitates, with their enhanced density for the sample N201 relative to N220 one. Analysis of FTIR spectra also indirectly confirmed the prevailing of the p-type conductivity. The granular structure of bright spots which decorates Te inclusions might be attributed to carbon or oxygen complexes formed nearby surface.

3. I–V characteristics

The I–V characteristics measured in dark and under steady state illumination, shown in Fig. 4, are inherent for the semi-insulating material. A small asymmetry of I–V branches measured in dark and attributed to forward and reverse applied voltages is observed which indicates existence of a Schottky barrier with a near-fully depleted volume even at small reverse voltages.

Steady-state illumination significantly increases the concentration of carriers within electrical neutral region leading to the enhanced asymmetry of the I–V branches (dash-curves in Fig. 4) attributed to forward and reverse applied voltages. However, this asymmetry is

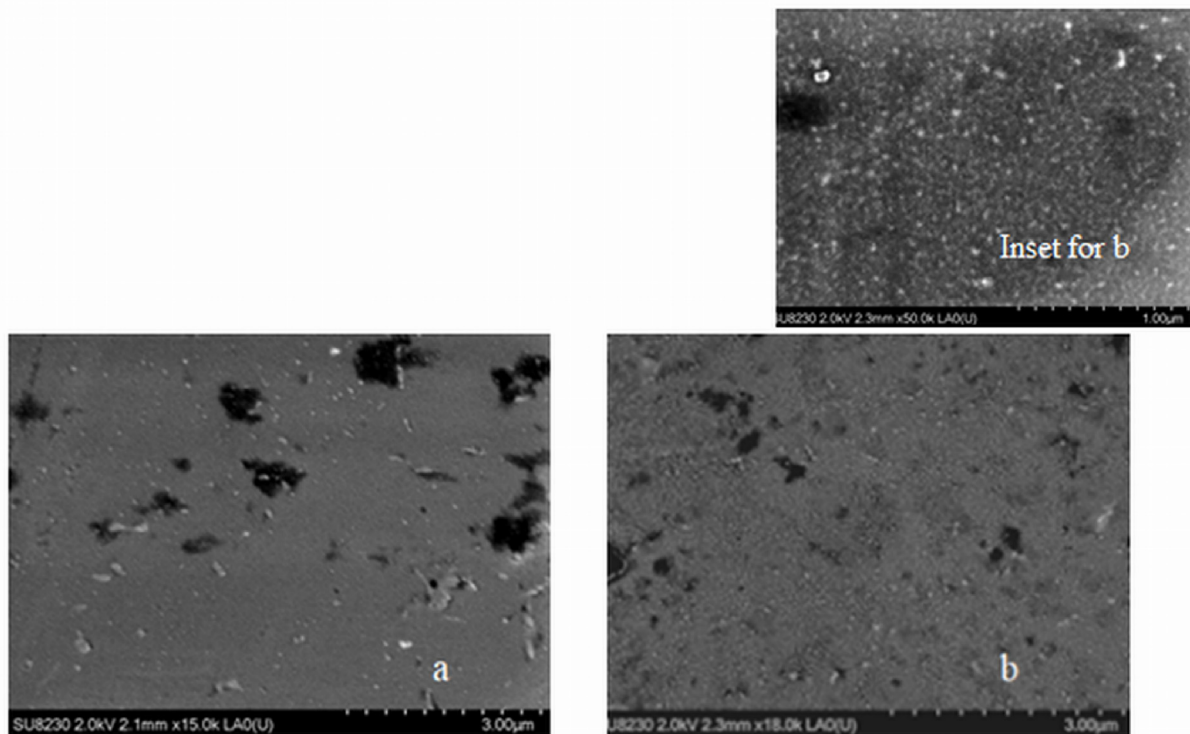


Fig. 3. SEM images taken for samples N220 (a) and N201 (b). The enlarged area of N201 sample with a granular structure is illustrated in the inset for Fig. b.

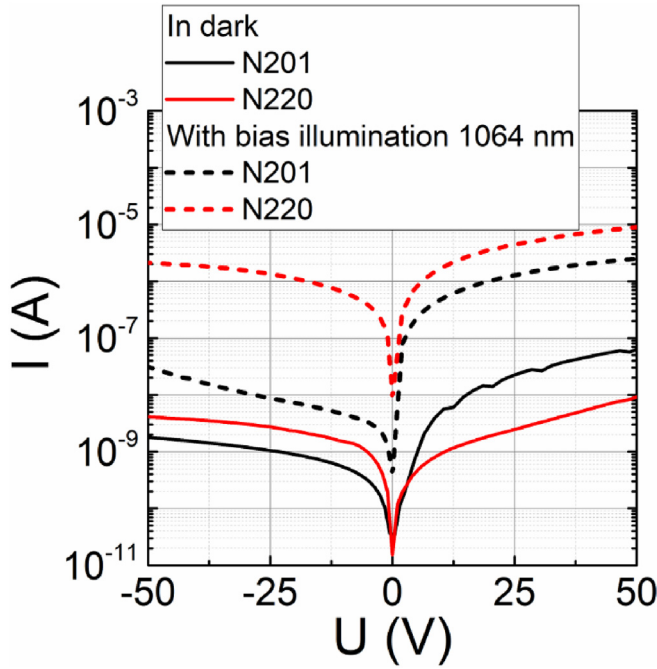


Fig. 4. I–V characteristics measured on N220 (red-curves) and N201 (black-curves) in dark (solid curves) and under illumination (dash –curves).

obtained to be stronger in samples of the N201 set relative to N220 ones. This implies the enhanced absorption of illumination in N201 samples which determines the larger concentration of steady-state excess carriers in the latter material and a narrower depletion region under illumination. The enhanced absorption might be related to the photo-active centres on surface and within bulk of N201 samples, in qualitative agreement with results of SEM imaging (Fig. 2) and EDXS data in Table 1.

4. BELIV characteristics

The hypothesis concerning Schottky diode full-depletion in dark, raised in explanation of I–V differences, has been corroborated by measurements of transients of the barrier evaluation characteristics using linearly increasing voltage (BELIV) [30–33].

4.1. BELIV method and instrumentation

The method of barrier evaluation by linearly increasing voltage (BELIV) [30–33] was applied to measure the pulsed currents (appearing due to charging/recharging of the barrier capacitance) in dark and under either steady-state or short laser pulse illumination. A setup of instrumentation for implementation of BELIV technique is illustrated in Fig. 5.

The BELIV technique for a reverse biased diode is based on analysis of the changes of barrier capacitance (C_b) with linearly increasing voltage $U_p(t) = At$ pulse. The variations of the barrier capacitance $C_b(t) = C_{b0}(1 + U(t)/U_{bi})^{-1/2}$ with voltage $U_p(t)$ determine a current pulse, measured on a load resistor, where barrier capacitance for a non-biased diode of an area S is $C_{b0} = \epsilon\epsilon_0 S/w_0 = (\epsilon\epsilon_0 S^2 e N_A / 2U_{bi})^{1/2}$. Here, such the symbols are employed: ϵ_0 is a vacuum permittivity, ϵ – material dielectric permittivity, e – elementary charge, U_{bi} – the built-in potential barrier, $w_0 = (2\epsilon\epsilon_0 U_{bi} / e N_A)^{1/2}$ – the width of depletion for the non-biased junction with dopant concentration N_A , $A = U_p/\tau_{PL}$ – the ramp of LIV pulse with a U_p peak amplitude and τ_{PL} duration.

The current transient $i_C(t)$ recorded using a load resistor R_L in the external circuit is represented (with precision of thermal potential) as:

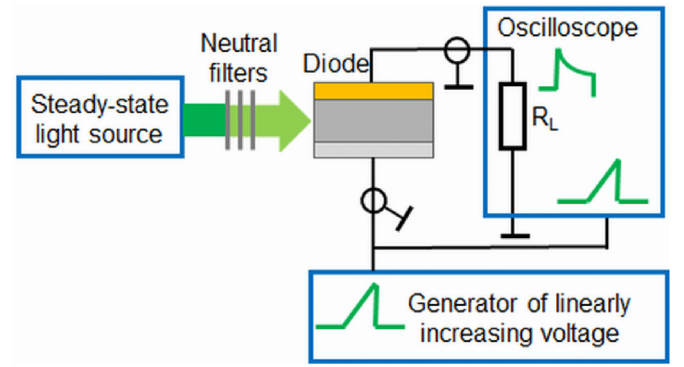


Fig. 5. Sketch of the arrangement of instruments for implementation of the BELIV technique.

$$i_C(t) = \frac{dq}{dt} = \begin{cases} \frac{\partial U}{\partial t} \left(C_b + U \frac{\partial C_b}{\partial U} \right) = \frac{\partial U_C}{\partial t} C_{b0} \frac{1 + \frac{U_C(t)}{2U_{bi}}}{\left(1 + \frac{U_C(t)}{U_{bi}}\right)^{3/2}} \approx AC_{b0} \frac{1 + \frac{At}{2U_{bi}}}{\left(1 + \frac{At}{U_{bi}}\right)^{3/2}}, & \text{at } U < U_{FD} \\ \frac{\partial U}{\partial t} (C_{geom} + U \frac{\partial C_{geom}}{\partial U}) = \frac{\partial U_C}{\partial t} C_{geom} \approx AC_{geom}, & \text{for } U \geq U_{FD} \end{cases} \quad (1)$$

The current transient for U_p voltages below $U_p < U_{FD}$ the full depletion voltage (U_{FD}) contains an initial ($t = 0$) step AC_{b0} due to displacement current and a descending component governed by the charge extraction. For an insulating material and for $U_p > U_{FD}$, this transient contains only a displacement current step. For the range of $0 < U_p \leq U_{FD}$, the transient contains a displacement current step and a descending charge extraction component. Values of N_A and U_{bi} can be deduced from the initial current expression $i_C(0) = AC_{b0}$, when delay $R_L C_b$ can be reduced to time-scale of the LIV pulse initial slope durations. The vertex amplitude within a BELIV transient is proportional to a value of a ramp A of LIV pulse, which is controlled by differentiating ($dU_p/dt = A$) the LIV pulse ($U_p(t)$), routinely controlled on screen of an oscilloscope. The diffusion current may be a reason in formation of a pedestal for $i_C(t)$ changes. The peak value of the $i_C(t)$ is a reciprocal of the depletion width (formed by the photo-excited free-carriers) and, thereby, it is proportional to the excess carrier concentration at the moment of appearance of a LIV pulse within the scanning sequence of LIV pulses. The excess carriers determine an appearance of the diode-inherent BELIV transients, while the changes of the shape and components of these transients indicate manifestation of carrier recombination and thermal emission centres.

4.2. Capacitance and conductivity characteristics

The role of the large serial resistance ascribed to the electrically neutral region (ENR) can be governed (considerably reduced) by varied intensity of the photo-injection of excess carriers. A device exhibits the capacitor like BELIV transient (a square-wave pulse) when recorded in dark (Fig. 6 a, the black curve 1 with the smallest amplitude). The steady-state illumination with increasing intensity (by using properly absorbed light wavelength) leads to appearance and evolution of the current within the diode-inherent BELIV transients (Fig. 6, curves 2–7) for partial depletion regime, - these transients for a rather small peak voltage U_p contain an initial ($t = 0$) current step $i(t = 0) = AC_{b0}$ ascribed to the displacement current and a descending component governed by the charge extraction. Due to $\tau_{RL} = R_L C_{b0}$ initial delay in the external circuit (with a load resistance R_L) or $\tau_{RS} = R_s C_{b0}$ caused by a

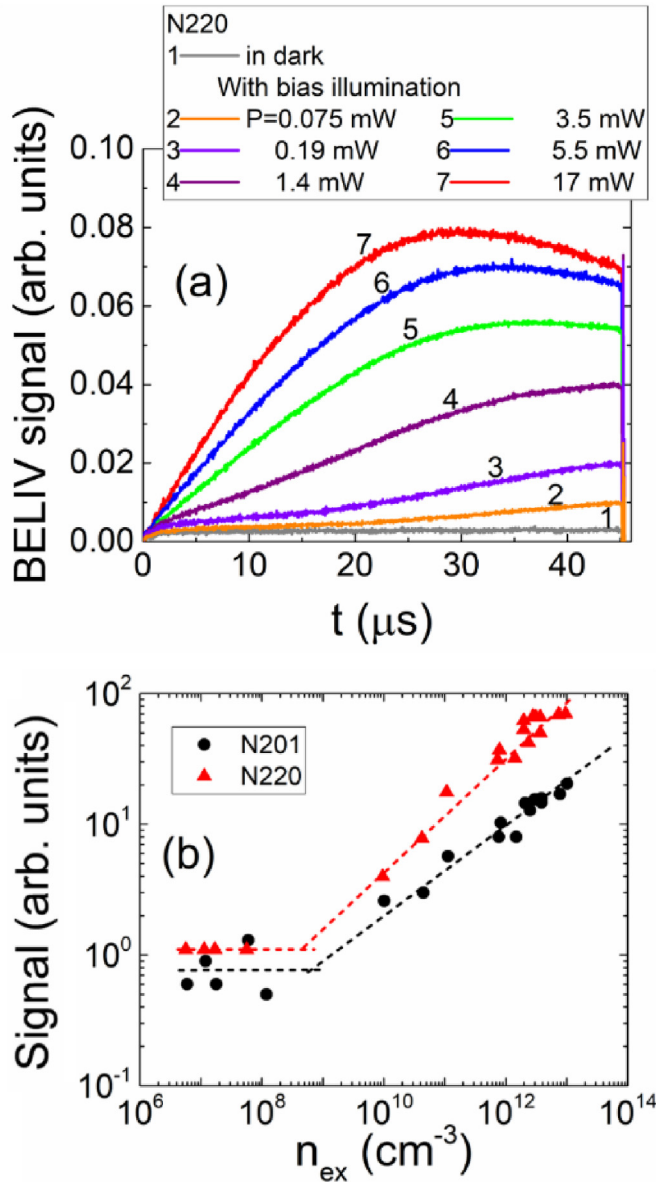


Fig. 6. Evolution of the BELIV transients recorded for the reverse polarity of applied voltage in sample N220 (a) and comparison of the peak currents recorded in samples N201 as well as N220 as a function of excess carrier concentration (b).

serial resistance R_s of the material within electrically neutral region (ENR), this initial step acquires a peak shape (Fig. 6, curves 2–7). Variations of the serial resistance due to excess carrier recombination (with carrier lifetime τ_R) can be a reason for the non-linear increase of BELIV current within barrier capacitance charging when rather short LIV ($\tau_p \sim \tau_R$) pulses are employed. The amplitude of the current increases with excitation intensity (power), while a delay time increases with reduction of the excitation intensity. The long delay times at reduced illumination intensity eventually lead to a formation of pulses with a long rise-to-vertex initial component. Further reduction of the intensity of the steady-state illumination intensity determines approaching of the diode-inherent BELIV transients to that of a pure square-wave shape, typical for a capacitor, - namely, to the recorded in dark BELIV transients (Fig. 6a, curve 1).

The latter values of the nearly stabilized charge extraction current, ascribed to barrier capacitance at a fixed moment of charge extraction, can serve for evaluation of the equilibrium carrier concentration in the

compensated (semi-insulating) material. Actually, depletion width w , for the fixed parameters of a LIV pulse, increases by approaching to a diode thickness d with reduction of the excess carrier concentration n_{ex} :

$$d \geq w = \left[\frac{2\epsilon\epsilon_0(U_{bi} + U_{p,LIV})}{e(N_{A,eff} + n_{\text{ex}})} \right]^{1/2} \quad (2)$$

Here, $N_{A,eff}$ is the effective dopant concentration. The compensation $\Delta K = p_0 - n_0$ of the prevailing dopants (for instance, acceptors of the N_A density at $p_0 > n_0$) can be expressed as [34]:

$$N_{A,eff} \approx \frac{N_A p_0 + \Delta K}{2 p_0} \quad (3)$$

The $N_{A,eff}$ approaches to zero with $n_0 \rightarrow 2p_0$. The limit to the depletion width w changes is equality in Eq. (2), i.e. $d = w_{FD}$, meaning full-depletion condition. It has been inferred from comparison of transients recorded on N220 and N201 samples (Fig. 6b) that equilibrium carrier concentration in samples N201 slightly exceeds that of N220 ones. The interception points of the peak current lines ascribed to fully depleted (capacitor-like) and partially depleted (diode-like) regimes set the effective doping density ($N_{A,eff}$) in the compensated (semi-insulating) material. An equality $d = w_{FD}$, meaning full-depletion condition appears as the transition point in the curve of the BELIV signal dependence on steady-state illumination power, where the branch of the decreasing BELIV signal with illumination power hops over the plateau curve branch (Fig. 6b), at $p < N_{A,eff}$. This condition can be estimated as an intersection point for the derivatives to plateau and descending curve branches in Fig. 6b. It can be deduced from Fig. 6b that close values of $N_{A,eff} \approx (4-6) \times 10^8 \text{ cm}^{-3}$ are obtained for both type (N201 and N220) samples, while BELIV peak currents are obtained to be larger for samples N220.

The extrapolation to the initial time instants of the transient slopes, obtained for the partially depleted diode, and finding of the instant, at which peak current is reached within a transient, as sketched in Fig. 7a. This enables evaluation of the barrier capacitance and delay time for a fixed illumination intensity. The barrier capacitance increases with illumination intensity due to a shrinkage of depletion width with increase of carrier density (Fig. 7b). The delay time (an approach of the instant of current peak to the origin of a transient) decreases with serial resistance of the ENR with enhancement of excess carrier density, as illustrated in Fig. 7b, evaluated for sample N201.

Having estimated $\tau_{delay} = C_{b0} R_{ENR}$ and C_{b0} parameters, the conductivity σ dependence (shown in Fig. 7c) on the excess carrier density is obtained. The excess carrier density is independently evaluated from the calibration measurements of the impinging light beam energy density per single quantum energy at fixed excitation wavelength using the appropriate value of the material absorption coefficient. The slope of the conductivity $\sigma = e\Delta n_{\text{ex}}\mu$ curve as a function of Δn_{ex} allows to evaluate the mobility of the majority carriers, in this p-CZT case of holes. Values of hole mobilities of $\mu_{h,201} = 16 \text{ cm}^2/\text{Vs}$ and $\mu_{h,220} = 18 \text{ cm}^2/\text{Vs}$ have thereby been estimated for N201 and N220 samples, respectively, for carrier densities in the range of $\Delta n_{\text{ex}} \leq 6 \times 10^{12} \text{ cm}^{-3}$.

5. Carrier lifetime characteristics

Carrier recombination characteristics were examined by contactless technique of microwave probed-photoconductivity (MW-PC) transients [35].

The single exponential MW-PC decay (Fig. 8) has been observed for the sample N220 at bulk excitation, using 1062 nm wavelength laser pulses. This indicates that the linear recombination prevails (with a single slope of the transient displayed within semi-log scale). The effective carrier recombination lifetime of $\tau_R = 10 \mu\text{s}$ has been estimated at $\exp(-1)$ level for samples N220.

Very different, a two-componental MW-PC decay process has been observed for the N201 samples. This implies the non-linear multi-

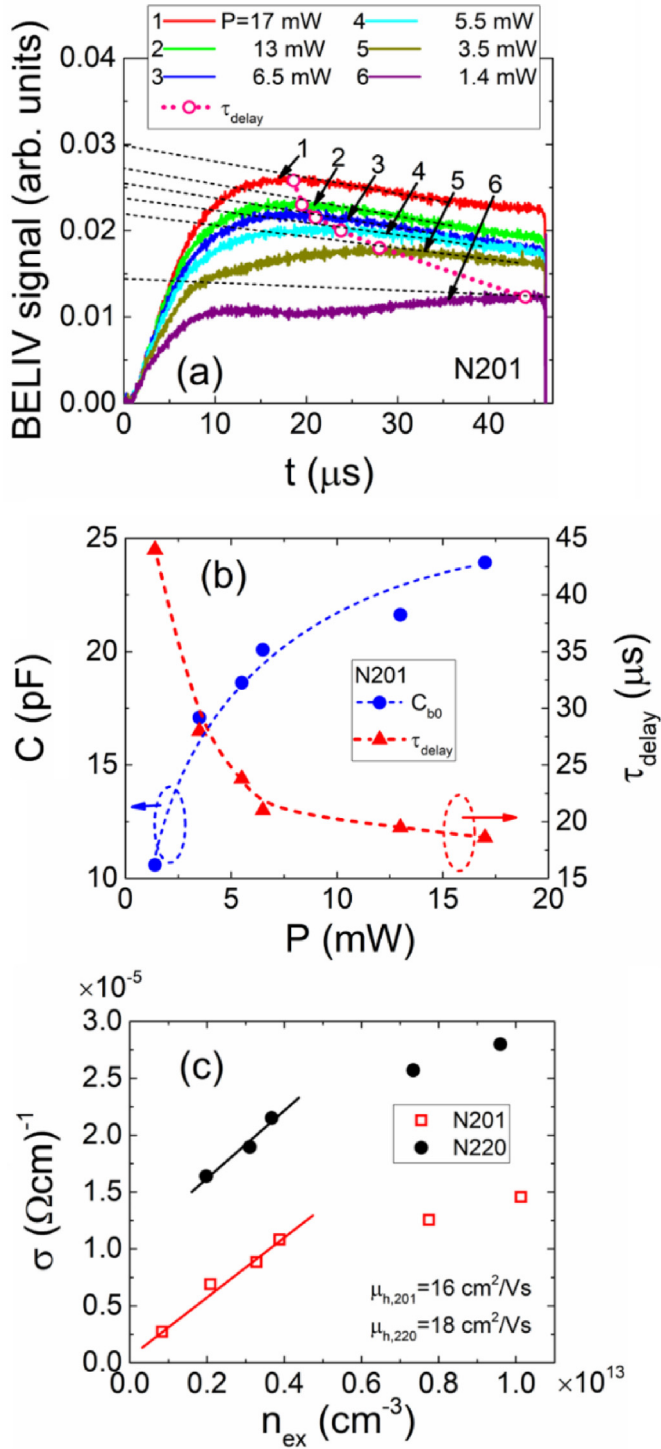


Fig. 7. (a) - Evolution of BELIV transients with power (P) of the steady-state illumination at $\lambda_{ex} = 532$ nm wavelength in N201 diodes. The dash curves and circles sketch the procedures of evaluation of the τ_{delay} , C_{b0} , R_{ENR} parameters. (b) - Barrier capacitance and delay time variations as a function of illumination power, obtained for the N201 sample. (c) Conductivity dependence on the excess carrier density evaluated for the N201 (open-square symbols) and N220 (solid circle symbols) samples.

trapping effect. This effect appears when lifetime dependence on excess carrier density during MW-PC decay is accounted for. This nonlinear decay process is characterized by instantaneous decay lifetime [35] through recombination lifetime and trapping coefficient K_{tr} as

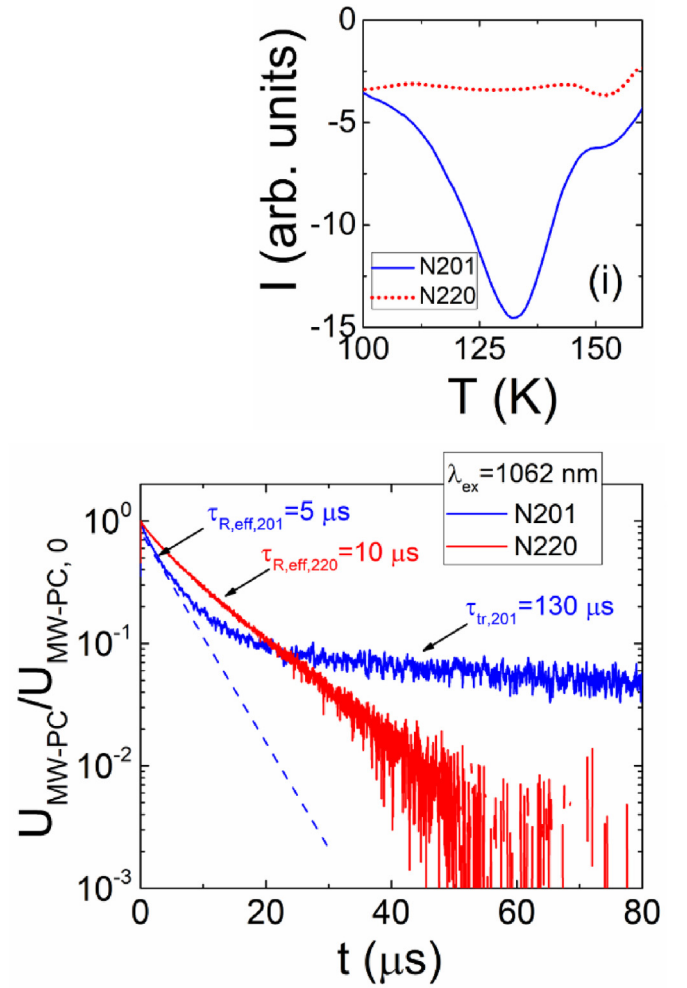


Fig. 8. The MW-PC transients normalized to a peak of the MW-PC response recorded on N201 and N220 samples using bulk excitation (1062 nm wavelength) by 400 ps laser pulses. In the inset (i), the O-I-DLTS spectra recorded on samples N201 and N220, ascribed to traps with activation energy of $\Delta E_{tr} = 0.21$ eV, are compared.

$$\tau_{inst,tr} = \tau_R K_{tr}; \quad K_{tr} = 1 + \frac{T_{tr} N_{C,V,e,h,Tr}}{(N_{C,V,e,h,Tr} + \Delta n)^2} \quad (4)$$

where T_{tr} is a concentration of shallow trapping centres, $N_{C,V,e,h,Tr} = N_{C,V,e,h} \exp(-\Delta E_{Tr}/kT)$ is the effective density of band states for trapped carriers, and Δn is the excess carrier density which are involved into trapping. The latter model leads to a quasi-exponential decay with time (t) dependent instantaneous lifetime $\tau_{inst,tr}(\Delta n(t))$ for the time instants when excess carrier density becomes lower than that generated from trapping centres, i. e. $\Delta n(t) \leq N_{C,V,e,h,Tr}$. This model describes the excitation density and temperature dependent variations of the rate of the recombination-trapping process [35]: recombination prevails within the initial stages of transients when $\Delta n \gg N_{C,V,e,h,Tr}$. Thus, a significant trapping effect can be verified and suppressed by varying the excitation density.

The recombination lifetime is commonly estimated from the slope of the initial decay stage. It has been deduced from Fig. 8 the effective recombination lifetime of $\tau_R = 5 \mu$ s in sample N201, which is twice shorter than that for N220 sample. The instantaneous trapping lifetime of 130μ s has been evaluated from the slope of asymptotic decay component. This leads to the value of trapping coefficient $K_{tr} \approx 26$. On the other hand, assuming that asymptotic decay process is governed by the de-trapped carriers at $\Delta n(t) \sim 0.01 N_{C,V,e,h,Tr}$ (approximated by extrapolating recombination ascribed decay, dash line in Fig. 8, which

indicates the instant of $\sim 30 \mu\text{s}$), value of trapping coefficient $K_{tr} \approx 28$ can be estimated. This leads to a simplified relation of $K_{tr} \approx (1 + T_{tr}/N_{C,V,e,h,T_{tr}})$ with $T_{tr}/N_{C,V,e,h,T_{tr}} = 27$. Then, the ratio $T_{tr} \exp(\Delta E_{tr}/k_B T)/N_{C,V}$ characterizes the prevailing trapping centres. The concentration of trapping centres $T_{tr,h} \approx 3 \times 10^{14} \text{ cm}^{-3}$ is estimated, using values $N_{C,V} = (0.7-4) \times 10^{18} \text{ cm}^{-3}$ and the most shallow traps with activation energy of $\Delta E_{tr} = 0.21 \text{ eV}$, extracted from DLTS spectra (inset for Fig. 8), recorded on sample N201 [36]. These trapping centres can be ascribed to Te precipitates. The rather high density of these traps seem to play the main role in photoconductivity quenching and the decrease of detector performance in N201 samples. To scan location (near surface or bulk) of these centres, the surface recombination velocity was measured.

6. Extraction of surface recombination parameters by MW-PC transient technique

Manifestation of the surface recombination phenomenon is determined by reduction of the amplitude A_1 of the main decay mode [35] with effective excitation depth, which is a reciprocal quantity relative to an absorption coefficient α . The absorption coefficient sharply increases with excitation photon energy on the absorption edge of CdZnTe material in the range of wavelengths of about 800–1000 nm [37].

The carrier density variation in time t and over wafer depth-coordinate x is described [35] by relation

$$n(x, t) = n_0 \sum_{m=1}^{\infty} A_m e^{-(D\eta_m^2 + 1/\tau_R)t} \sin\left(\eta_m x + \arctg \frac{D\eta_m}{s}\right) \quad (5)$$

where n_0 is the concentration of the light injected excess carrier pairs, A_m is the decay amplitude ascribed to the spatial frequency η_m of the m -th decay mode, τ_R is the bulk recombination lifetime, D is the coefficient of ambipolar diffusion of carriers, s is the velocity of surface recombination. Carrier decays within initial phase (Fig. 9) hint on a non-exponential decay process at the depth-inhomogeneous excitation. The averaged carrier pair concentration over the layer thickness d and normalized to its peak value (at $t = 0$) changes in time as

$$\frac{\langle n(t) \rangle_d}{\langle n(0) \rangle_d} = \sum_{m=1}^{\infty} \langle A_m \rangle_d e^{-(D\eta_m^2 + 1/\tau_R)t} \quad (6)$$

The spatial frequencies for equal velocities ($s_1 = s_2 = s$) of recombination on opposite surfaces (due to the same surface preparing procedures) can be determined by solving the transcendental equation

$$\text{ctg}(\eta d) = \eta d \frac{D}{s} \quad (7)$$

The expression for the peak amplitude A_m of the m -th decay mode is obtained as

$$\langle A_m \rangle_d = \frac{8}{(\eta_m d)^2 (1 + (\frac{D}{sd})^2 (\eta_m d)^2 + 2 \frac{D}{sd})} \frac{\alpha d/2}{1 + (\alpha d/\eta_m d)^2} \left(\text{cth} \frac{\alpha d}{2} + \frac{D\alpha}{s} \right) \quad (8)$$

The effective decay time, measured in the asymptote of a transient, is then expressed as

$$\tau_{eff}^{-1} = \tau_R^{-1} + \frac{D(\eta_1 d)^2}{d^2} \quad (9)$$

For extraction of values of surface recombination velocity, two equations (Eqs. (7) and (8)), containing parameters s and D , are exploited. Consequently, the peak amplitude $A_{m=1}$ (shown in Fig. 9 as an intersection of the prolonged asymptotic decay slope with ordinate axes) ascribed to the main decay mode $\eta_1 = \eta_{m=1}$ can be simulated as a function of the dimensionless surface recombination parameter $S = sd/D$ using the one-dimensional diffusion approximation. For a reliable

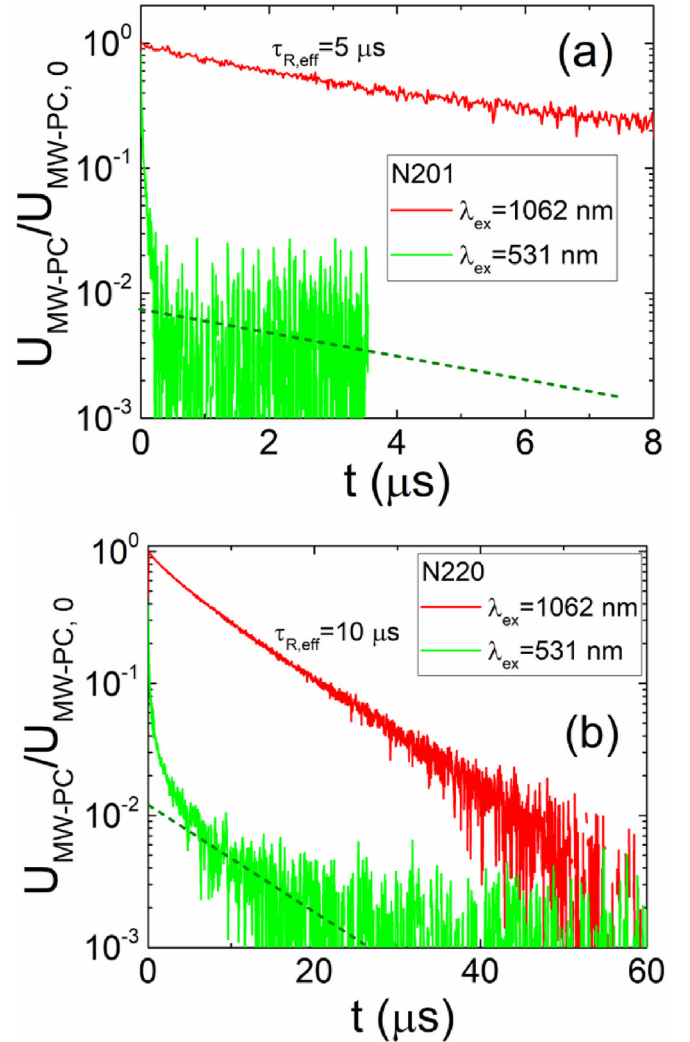


Fig. 9. Comparison of the MW-PC transients normalized to a peak of the MW-PC response recorded on N201 (a) and N220 (b) samples using bulk excitation (1062 nm wavelength) and surface excitation (531 nm wavelength) by 400 ps laser pulses.

evaluation of the $A_{m=1}(\eta_{m=1}(s))$ and the asymptotic decay lifetime $\tau_{eff}(\eta_1(s), \tau_R)$, two excitation wavelengths are employed: the considerable reduction of the amplitude ($A_{m=1}(\alpha, \eta_1(s))$) of the main decay mode η_1 is clearly observed in Fig. 9 using surface excitation regime, while τ_{eff} is measured most precisely for bulk excitation. Having evaluated A_1 for known ad and D , the parameter s is directly extracted.

It has been inferred from Fig. 9 that velocity of surface recombination extracted for samples N201 exceeds that for N220 material, as initial decay component obtained for N201 sample is significantly shorter than that for N220 one. Additionally, values of $\langle A_{m=1} \rangle$ for samples N201 are less than that obtained for N220 material.

At low excitation when equilibrium carrier concentration (acceptor concentration N_A in p-CdZnTe) prevails the excess carrier density, $n < N_A$, the ambipolar diffusion coefficient D approaches to that $D_p = 2 \text{ cm}^2/\text{s}$ of holes. Values of D_p were estimated using mobility values estimated by BELIV technique and Einstein's relation. Assuming these values of D_p parameter, the surface recombination velocity values of $s_{N220} = 1.7 \times 10^3 \text{ cm/s}$ and $s_{N201} = 3.7 \times 10^3 \text{ cm/s}$ have been extracted, respectively. The determined surface recombination velocity values $\sim (2-4) \times 10^3 \text{ cm/s}$ for both sets of samples imply rather good quality of surface preparation and show rather small difference between

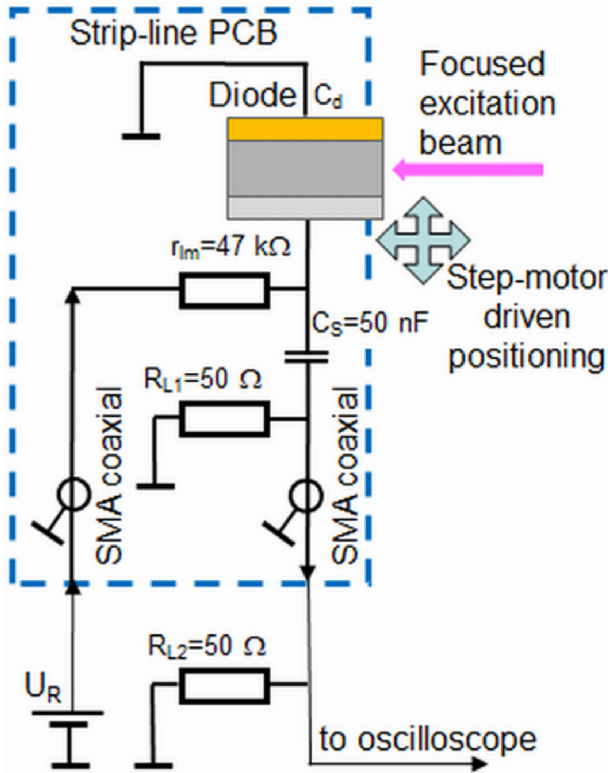


Fig. 10. A setup for the recording of injected charge current transients and for their profiling.

the examined CZT sets. This additionally indicates that trapping centres in N201 samples reside in diode bulk.

7. TCT and carrier mobility characteristics

Carrier transport parameters and detector operation characteristics have been examined by using pulsed transient current technique (TCT), implemented in the sample edge scanning regime.

7.1. Method and instrumentation

A transient current technique (TCT) is widely applied for characterization of ionizing radiation detectors [38–46]. This technique (actually implemented by measurements of the injected carrier drift currents (ICDC)) is based on recording of current transients determined by the carrier drift-diffusion-recombination processes within inter-electrode gap due to the excess carriers induced by focused laser beam using diode boundary edge excitation (Fig. 10).

An electrical circuitry, sketched in Fig. 10, was employed, and measurements at room temperature were performed. Here, the $r_{lm} = 47 \text{ k}\Omega$ resistance is used for limitation of the charging current (for a $C_s = 50 \text{ nF}$ capacitor). The diode with barrier capacitance C_d under test (CUD) is connected in series with direct current (DC) voltage U_R source and r_{lm} . A circuit for pulsed signal is then comprised of the diode and the load resistor $R_{L1} = 50 \Omega$ (on input of coaxial cable) connected in series. These elements C_d , C_s , and R_{L1} are mounted on the strip-line PCB. The 50Ω coaxial cable is loaded by $R_{L2} = 50 \Omega$ on its output and at input of a 2 GHz band digital oscilloscope LeCroy Wave Runner 620Zi, to get equivalent $R_L = R_{L1} || R_{L2} = 25 \Omega$. A closed input of the oscilloscope is discriminated by a few pF capacitor from the DC signals. A 500 ps pulsed STA-01 laser was used as an excitation source at 1062 nm wavelength. The perpendicular experimental geometry (Fig. 10, when excitation beam impinges perpendicularly to an applied electrical field direction) was employed. The injected charge drift

current (ICDC) transients are profiled either by varying the reverse-bias DC voltage or scanning position of the cylindrical-lens slit-focused laser beam.

Description of the currents induced by the injected carrier capture and drift in junction type sensors can be found in Refs. [42–46]. This model has been used for interpretation of current transients. The instantaneous current values depend on the injected charge amount and on transit time which is consequently determined by the characteristic times of dielectric relaxation $\tau_{Mq, e, h} = \epsilon_0 \epsilon d / q_{e, h} \mu_{e, h}$ and of free flight $\tau_{TOF, e, h} = d^2 / U \mu_{e, h}$ of the sub-domains of injected carriers with mobilities $\mu_{e, h}$. This current also depends on time variations of the instantaneous positions of sub-domains ($\psi_{e, h}(t)$). The expression for current variations in time, determined by carrier drift and capture processes, can be represented as

$$i(t) = \frac{d\sigma}{dt} S = \left[-\frac{\partial q_e(t)}{\partial t} (1 - \psi_e(t)) - q_e(t) \frac{d\psi_e(t)}{dt} - \frac{\partial q_h(t)}{\partial t} \psi_h(t) - q_h(t) \frac{d\psi_h(t)}{dt} \right] S \quad (10)$$

for the mixed drift regime, containing stages of the bipolar and monopolar drift. In the case of pure bipolar drift, a drift velocity appears to be invariable due to $\psi_{e, h}(t) \sim t$. This leads to a square-wave shape of the current pulse. The real evolution (the rise to peak) of the current should be considered by including the process of the barrier capacitance charging. Current decreases after the initial peak for the mixed drift regime due to a drag of the late arrived sub-domain by the counter-partner sub-domain. The later phase of the monopolar drift only contains the increasing (if $\tau_{TOF, h} = \tau_{Mq, h}$) or nearly constant (if $\tau_{TOF, h} < \tau_{Mq, h}$) component of velocity. Thereby the double-peak current pulse can be inherent for the mixed (a bipolar changed by a monopolar) drift regime. A duration of the double-peak current pulses significantly varies depending on the external voltage and excess carrier injection position. A duration of the TCT/ICDC pulse (single-peak shape) is also nearly independent of the applied voltage when carrier capture-recombination processes ($\partial q_{e, h} / \partial t$ terms in Eq. (10)) prevail.

7.2. Depth and voltage scan characteristics

Variations of the edge-TCT transients are illustrated in Fig. 11 (a) and (c) for diodes N201 and N220, respectively. These characteristics are qualitatively similar for both sets of diodes.

Variation of the TCT transients, dependent on the applied voltage and recorded for the sample N201 at near contact injection, is illustrated in Fig. 11a. The shortening of the carrier transit time as well as TCT pulse (denoted by open circles) with enhancement of voltage is clearly observed. The double peak-shape is inherent for rather small voltages, when both bipolar and monopolar drift components can be implied. Then, the current component ascribed to the hole drift to ohmic electrode is observable together with electron drift to Schottky barrier. The latter current, associated with the monopolar electron drift component, may exceed that of the hole drift due to large asymmetry in hole and electron mobilities in CZT materials. Therefore, electron drift velocity is more than ten times larger than that of hole drift, and, the displacement current, which is proportional to drift velocity, prevails for electrons. With enhancement of voltage, the electron component becomes short.

The transit time serves for evaluation of drift mobility μ . This parameter can be estimated from the slope of μ versus U_R^{-1} characteristics, shown in Fig. 11 b. The electron dominated drift mobility has been evaluated to be $\mu_e = 1190 \text{ cm}^2/\text{Vs}$ for N201 samples and $1240 \text{ cm}^2/\text{Vs}$ for N220 samples, respectively. Precision of estimation of the hole drift component is insufficient for these edge TCT transients. Unfortunately, the hole mobility estimation accuracy even falls down with enhancement of injection location. It can be inferred from

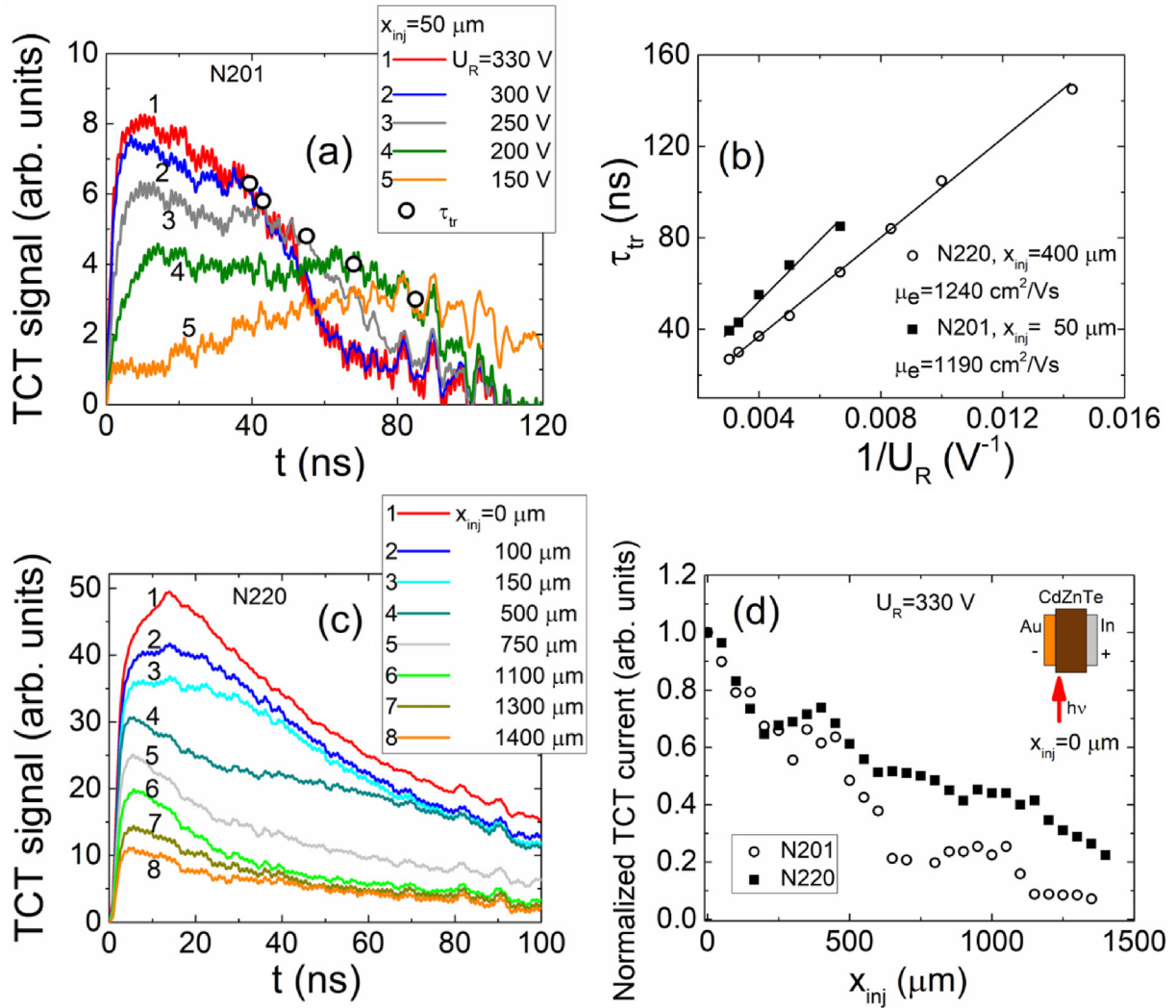


Fig. 11. Edge-TCT transients, dependent on applied bias voltage, recorded for Schottky diode N201 (a), and transit time as a function of the reverse voltage measured in samples N201 and N220 (b). Variation of transients within TCT depth-scan in sample N220 obtained at reverse voltage of 330 V (c) and TCT peak-current variations with injection location (x_{inj}) recorded in samples N201 and N220 (d).

Fig. 11b, that values of electron mobility are close for both N201 and N220 materials.

Evolution of transients, recorded in sample N220 varying excess carrier domain injection, is illustrated in Fig. 11c. It can be deduced from Fig. 11c that peak current decreases with injection location approach to junction, when applied voltage is kept fixed. This can be explained by carrier trapping and recombination during drift process. On the other hand, it can be noticed that duration of TCT-pulse and transit time varies within depth-scan: the shortest pulses are observed for the injection locations nearby contacts, while the longest drift is observed when carrier domain is injected in the middle of sample thickness. This is inherent peculiarity of bipolar drift [43,45].

The profiles of edge-TCT peak currents, illustrated in Fig. 11d, indicate some non-monotone in current decrease with approach to contacts. The larger current jumps within these profiles have been observed for samples N201 relative to that of N220. The current spikes might be explained by depth inhomogeneity of carrier traps and scattering centres.

8. Discussion

The clear difference in recorded ^{137}Cs (using the same test conditions: detector operating voltage of 600 V, gamma-radiation field with

dose rate of about 0.5 Sv/h) radiation spectra in diode sets of N201 and N220 seems to be caused by defects residing in these materials, as narrow XRD reflexes indicate perfect single-crystal quality of both materials. The content index of $x = 0.12$ in ternary compound of $\text{Cd}_{1-x}\text{Zn}_x\text{Te}$ was estimated by combining XRD and EDXS data. The SEM images implies difference in density and size of Te inclusions. Also, EDXS spectra point on the enhanced amount of oxygen and carbon impurities within N201 samples relative to that in N220 ones, as listed in Table 1.

The I-V and BELIV characteristics clearly show the large resistivity of both materials. The dark concentration of carriers and thereby dopant effective density, listed in Table 2, was estimated to be in the range of $(4-6) \times 10^8 \text{ cm}^{-3}$ by scanning BELIV transients with varied intensity of additional steady-state illumination. This implies the effective density of dopants $N_{A,eff} \sim 5 \times 10^8 \text{ cm}^{-3}$ leading to the p-type of material conductivity, which was corroborated by polarity of applied voltage causing depletion regime in I-V and BELIV responses. Also, using measurements of the photo-conductivity in electrical neutral region (ENR) and analysis of the BELIV transients, dependent on excess carrier density, the hole mobility has been estimated. The hole mobility values were found to be of the order of $16-18 \text{ cm}^2/\text{Vs}$, and close (Table 2) for both N201 and N220 diodes. The appearance of the trapping effect was the main difference between N201 and N220 diode sets in

Table 2
Parameters evaluated in diode sets by combining electrical characterization techniques.

Sample	$N_{A,eff}$ (cm ⁻³)	$\tau_{R,eff}$ (μ s)	τ_{tr} (μ s)	K_{tr}	N_{tr} (cm ⁻³)	s (cm/s)	μ_e (cm ² /Vs)	μ_h (cm ² /Vs)
N201	6×10^8	5	130	27	$\sim 3 \times 10^{14}$	3.7×10^3	1190	16
N220	4×10^8	10	–	–	–	1.7×10^3	1240	18

measurements of microwave-probed photoconductivity transients. This effect was found to be inherent only for the diodes N201. The rather long instantaneous trapping lifetime of the $\tau_{tr} = 130 \mu$ s indicated trapping coefficient of the order $K_{tr} = 27$. Assuming values of the effective density of states, inherent for CdTe and CZT materials, the concentration of trapping centres has been estimated to be $3 \times 10^{14} \text{ cm}^{-3}$ employing parameters of the most shallow thermal emission centres with activation energy of 0.21 eV, extracted from the DLTS spectroscopy, performed on N201 samples. These trapping centre concentrations exceed the dopant density by several orders of magnitude. The trapping centres might be associated with Te_{Cd} as well as V_{Cd}^{0/-} point defects and Te inclusions. The latter hypothesis is in line with SEM imaging data. It is probable that these trapping centres reside in bulk of the N201 diodes, as surface recombination velocity was found to be rather small (of the order of magnitude $s = (2-4) \times 10^3 \text{ cm/s}$, Table 2) with close values for both N220 and N201 samples. Values of s additionally testify a good quality of surface preparation. The effective recombination lifetime in bulk of N201 samples is also twice shorter than that for N220 ones (Table 2). However, such a difference in bulk recombination lifetimes is hardly responsible for the significant difference in detector performance. Also, values of electron mobility $\mu_e \sim 1200 \text{ cm}^2/\text{Vs}$, extracted from edge-TCT profiling, are close for both N201 and N220 samples. This complementarily evidences the rather high crystalline quality of these materials. Nevertheless, the processes of recombination might be a reason for the non-monotonous and descending current profiles observed within edge-TCT scans. The $\mu_e \tau_{R,eff}$ product of the order of $10^{-2} \text{ cm}^2/\text{V}$ has thereby been estimated, and this additionally testifies the rather good quality of the examined materials.

9. Summary

The comparative study of radiation detectors made of CdZnTe (CZT) materials and exhibiting good (N220) and unacceptable (N201) spectral performance has been performed by combining several electrical characterization techniques.

The single-crystal CZT material quality of both sample sets has been testified by XRD means. The SEM imaging together with EDXS spectroscopy showed the enhanced amount of impurity elements and Te inclusions, decorated with granular structure of additional defects, for the N201 set relative to that of N220 one.

The I–V and barrier capacitance pulsed transients showed high resistivity of both p-type CZT materials with carrier/dopant dark concentration of $N_{A,eff} \approx 5 \times 10^8 \text{ cm}^{-3}$. Analysis of barrier capacitance pulsed transients and profiling of the transient currents by scanning the charge domain injection on diode edge allowed to evaluate carrier mobility. The extracted values of $\mu_e \approx 1200 \text{ cm}^2/\text{Vs}$ and $\mu_h \approx 17 \text{ cm}^2/\text{Vs}$ for both materials show acceptable carrier transport parameters for implementing such the Schottky diodes for detection of the ionizing radiations. The carrier lifetime relative to bulk recombination was found to be $\tau_{R,eff} \approx 5 \mu$ s and 10μ s for N201 and N220 CZT samples, respectively. The $\mu_e \tau_{R,eff}$ product of the order of $10^{-2} \text{ cm}^2/\text{V}$ has been estimated, and this additionally testifies the rather good quality of the examined CZT materials. The surface recombination velocity values of $s = 4 \times 10^3 \text{ cm/s}$, measured by using MW-PC technique, also evidence the acceptable surface preparing. The difference of the mentioned above parameters for both sets of CZT samples falls within error bars of the evaluated parameters, therefore, the average values are here listed.

The main difference between the examined diodes appeared through carrier trapping effect, observable only for N201 diodes. The rather long instantaneous trapping lifetime of the $\tau_{tr} = 130 \mu$ s indicated trapping coefficient of the order $K_{tr} = 27$. The concentration of trapping centres has been estimated to be $> 3 \times 10^{14} \text{ cm}^{-3}$ of the most shallow thermal emission centres. These trapping centre concentrations exceed dopant density by several orders of magnitude. The trapping centres might be associated with Te_{Cd} as well as V_{Cd}^{0/-} point defects and Te inclusions, and the latter hypothesis is in line with SEM imaging data.

Acknowledgements

This research was partially supported by Lithuania Academy of Science under grant LMA-CERN -19.

References

- [1] M. Fiederle, C. Eiche, W. Joerger, M. Salk, A.S. Senchenkov, A.V. Egorov, D. Ebling, K.W. Benz, Radiation detector properties of CdTe_{0.9}Se_{0.1}:Cl crystals grown under microgravity in a rotating magnetic field, *J. Cryst. Growth* 166 (1996) 256.
- [2] T.E. Schlesinger, R.B. James, Semiconductors for Room Temperature Nuclear Detector Applications, Academic Press, 1995.
- [3] T.E. Schlesinger, J.E. Toney, H. Yoon, E.Y. Lee, B.A. Brunett, L. Franks, R.B. James, Cadmium zinc telluride and its use as a nuclear radiation detector material, *Mater. Sci. Eng. R Rep.* 32 (2001) 103.
- [4] K. Iniewski, CZT detector technology for medical imaging, *J. Instrum.* 9 (2014) C11001.
- [5] M. Streicher, S. Brown, Y. Zhu, D. Goodman, Z. He, S. Member, Special nuclear material characterization using digital 3-D position sensitive CdZnTe detectors and high purity germanium spectrometers, *IEEE Trans. Nucl. Sci.* 63 (2016) 2649.
- [6] A.S. Hoover, W. Baird, R.M. Kippen, M.W. Rawool-Sullivan, J.P. Sullivan, A Compton imaging device for radioactive material detection, *Optical Science and Technology SPIE's 49th Annual Meeting*, 2004 Denver, Colorado USA <https://permalink.lanl.gov/object/tr?what=info:lanl-repo/lareport/LA-UR-04-4500>, Accessed date: 13 June 2019.
- [7] D.M. Hofmann, P. Omring, H.G. Grimmeiss, B.K. Meyer, K.W. Benz, D. Sinerius, Identification of the chlorine A center in CdTe, *Phys. Rev. B* 45 (1992) 6247.
- [8] A. Zerrai, K. Cherkaoui, G. Marrakchi, G. Bremond, P. Fougeres, M. Hage-Ali, J.M. Koebel, P. Siffert, Influence of deep levels on CdZnTe nuclear detectors, *J. Cryst. Growth* 197 (1999) 646.
- [9] L. Verger, N. Baffert, M. Rosaz, J. Rustique, Characterization of CdZnTe and CdTe:Cl materials and their relationship to X- and γ -ray detector performance, *Nucl. Instrum. Methods Phys. Res. A* 380 (1996) 121.
- [10] P. Fougeres, M. Hage-Ali, J.M. Koebel, P. Siffert, S. Hassan, et al., Properties of CdZnTe crystals grown by high pressure Bridgman for nuclear detection, *J. Cryst. Growth* 184/185 (1998) 1313.
- [11] M. Fiederle, T. Feltgen, J. Meinhardt, M. Rogalla, K.W. Benz, State of the art of (Cd,Zn)Te as gamma detector, *J. Cryst. Growth* 197 (1999) 635.
- [12] R. Nan, T. Wang, G. Xu, M. Zhu, W. Jie, Compensation processes in high-resistivity CdZnTe crystals doped with In/Al, *J. Cryst. Growth* 451 (2016) 150.
- [13] Q. Li, W. Jie, L. Fu, G. Yang, G. Zha, T. Wang, D. Zeng, Photoluminescence analysis on the indium doped Cd_{0.9}Zn_{0.1}Te crystal, *J. Appl. Phys.* 100 (2006) 013518.
- [14] G. Yang, W. Jie, Q. Li, T. Wang, G. Li, H. Hua, Effects of indium doping on the properties of CdZnTe single crystals, *J. Cryst. Growth* 283 (2005) 431.
- [15] W. Stadler, D.M. Hofmann, H.C. Alt, T. Muschik, B.K. Meyer, E. Weigel, G. Müller-Vogt, M. Salk, E. Rupp, K.W. Benz, Optical investigations of defects in Cd_{1-x}Zn_xTe, *Phys. Rev. B* 51 (1995) 10619.
- [16] A. Castaldini, A. Cavallini, B. Fraboni, L. Polenta, P. Fernandez, J. Piqueras, Cathodoluminescence and photoinduced current spectroscopy studies of defects in Cd_{0.8}Zn_{0.2}Te, *Phys. Rev. B Condens. Matter* 54 (1996) 7622.
- [17] M. Fiederle, C. Eiche, W. Joerger, M. Salk, A.S. Senchenkov, A.V. Egorov, D. Ebling, K.W. Benz, Radiation detector properties of CdTe_{0.9}Se_{0.1}:Cl crystals grown under microgravity in a rotating magnetic field, *J. Cryst. Growth* 166 (1996) 256.
- [18] T. Kunz, M. Laasch, J. Meinhardt, K.W. Benz, CdTe and CdTe:Cl vapour growth in a semi-closed system, *J. Cryst. Growth* 184–185 (1998) 1005.
- [19] C. Eiche, D. Maier, D. Sinerius, J. Weese, K.W. Benz, J. Honerkamp, Investigation of compensation defects in CdTe:Cl samples grown by different techniques, *J. Appl. Phys.* 74 (1993) 6667.
- [20] U. Pal, P. Fernández, J. Piqueras, N.V. Sochinskii, E. Diéguez, Cathodoluminescence characterization of Ge-doped CdTe crystals, *J. Appl. Phys.* 78 (1995) 1992.
- [21] A. Castaldini, A. Cavallini, B. Fraboni, P. Fernandez, J. Piqueras, Deep energy levels

- in CdTe and CdZnTe, *J. Appl. Phys.* 83 (1998) 2121.
- [22] K. Suzuki, K. Inagaki, N. Kimura, I. Tsubono, T. Sawada, K. Imai, S. Seto, Doping induced defects of $\text{Cd}_{1-x}\text{Zn}_x\text{Te}$ grown from Te solution, *Phys. Status Solidi A-Appl. Mat.* 147 (1995) 203.
- [23] L.C. Isett, P.K. Raychaudhuri, Deep levels in n -CdTe, *J. Appl. Phys.* 55 (1984) 3605.
- [24] M. Samimi, B. Biglari, M. Hage-Ali, J.M. Koebel, P. Siffert, About the origin of the 0.15 to 0.20 eV defect level in cadmium telluride, *Phys. Status Solidi A-Appl. Mat.* 100 (1987) 251.
- [25] C. Szeles, D. Bale, J. Grosholz, G.L. Smith, M. Blostein, J. Eger, Fabrication of high performance CdZnTe quasi-hemispherical gamma-ray CAPtureTM Plus detectors, in: L.A. Franks, A. Burger, R.B. James (Eds.), *Hard X-Ray and Gamma-Ray Detector Physics VIII*, Proceedings of SPIE, vol. 6319, SPIE, Bellingham, 2006.
- [26] V. Ivanov, P. Dorogov, A. Loutchansky, L. Grigorjeva, D. Millers, Improving the performance of quasi-hemispherical CdZnTe detectors using infrared stimulation, *IEEE Trans. Nucl. Sci.* 59 (2012) 2375.
- [27] Z. Liang, J. Min, S. Yang, et al., Cooling process optimization to control Te inclusions for improving CdZnTe detector performance, *Mater. Sci. Semicond. Process.* 30 (2015) 14.
- [28] A.E. Bolotnikov, G.S. Camarda, G.A. Carini, Y. Cui, K.T. Kohman, L. Li, M.B. Salomon, R.B. James, Performance-limiting defects in CdZnTe detectors, *IEEE Trans. Nucl. Sci.* 54 (2007) 821.
- [29] G.S. Camarda, A.E. Bolotnikov, G.A. Carini, Y. Cui, K.T. Kohman, L. Li, R.B. James, High spatial-resolution imaging of Te inclusions in CZT material, in: L.A. Franks, A. Burger, R.B. James (Eds.), *Hard X-Ray and Gamma-Ray Detector Physics VIII*, Proceedings of SPIE, vol. 6319, SPIE, Bellingham, 2006.
- [30] E. Gaubas, T. Čeponis, S. Sakalauskas, A. Uleckas, A. Velička, Fluence dependent variations of barrier and generation currents in neutron and proton irradiated Si particle detectors, *Lithuanian J. Phys.* 51 (2011) 227.
- [31] E. Gaubas, T. Čeponis, A. Uleckas, R. Grigonis, Room temperature spectroscopy of deep levels in junction structures using barrier capacitance charging current transients, *J. Instrum.* 7 (2012) P01003.
- [32] E. Gaubas, T. Čeponis, V. Kalendra, J. Kusakovskij, A. Uleckas, Barrier evaluation by linearly increasing voltage technique applied to Si solar cells and irradiated pin diodes, *ISRN Materials Science* (2012) 543790 2012.
- [33] E. Gaubas, T. Čeponis, J. Vaitkus, Pulsed Capacitance Technique for Evaluation of Barrier Structures, LAMBERT Academic Publishing, Berlin, 2013.
- [34] S.M. Ryvkin, *Photoelectric Effects in Semiconductors*, Consultants Bureau, New York, 1963.
- [35] E. Gaubas, E. Simoen, J. Vanhellemont, Review - carrier lifetime spectroscopy for defect characterisation in semiconductor materials and devices, *ECS J. Solid State Sci. Technol.* 5 (2016) P3108.
- [36] E. Gaubas et al. Defect Spectroscopy in CZT Diodes, -will Be Published Elsewhere.
- [37] R.O. Bell, Review of optical applications of CdTe, *Rev. Phys. Appl.* 12 (1977) 391.
- [38] H. Spieler, *Semiconductor Detector Systems*, Oxford University Press, Oxford, 2005.
- [39] G. Kramberger, Edge-TCT studies of irradiated HVCMOS sensor, Presentation at 25th Rd50 Workshop, 2014 Geneva www.cern.ch/rd50, Accessed date: 13 June 2019.
- [40] V. Eremin, N. Strokan, E. Verbitskaya, Z. Li, Development of transient current and charge techniques for the measurement of effective net concentration of ionized charges (N_{eff}) in the space charge region of p-n junction detectors, *Nucl. Instrum. Methods A* 372 (1996) 388.
- [41] V. Eremin, E. Verbitskaya, Z. Li, The origin of double peak electric field distribution in heavily irradiated silicon detectors, *Nucl. Instrum. Methods A* 476 (2002) 556.
- [42] E. Gaubas, T. Čeponis, J. Pavlov, Pulsed current signals in capacitor type particle detectors, *J. Instrum.* 10 (2015) C01006.
- [43] E. Gaubas, T. Čeponis, V. Kalesinskas, J. Pavlov, J. Vysniauskas, Simulations of operation dynamics of different type GaN particle sensors, *Sensors* 15 (2015) 5429.
- [44] E. Gaubas, T. Čeponis, A. Jasiunas, V. Kalendra, J. Pavlov, N. Kazuchits, E. Naumchik, M. Rusetsky, Lateral scan profiles of the recombination parameters correlated with distribution of grown-in impurities in HPHT diamond, *Diam. Relat. Mater.* 47 (2014) 15.
- [45] E. Gaubas, T. Čeponis, V. Kalesinskas, Currents induced by injected charge in junction detectors, *Sensors* 13 (2013) 12295.
- [46] E. Gaubas, T. Čeponis, D. Meskauskaitė, N. Kazuchits, Profiling of current transients in capacitor type diamond sensors, *Sensors* 15 (2015) 13424.